Experimental Investigation on the Wake Characteristics and Aeromechanics of Dual-Rotor Wind Turbines

Ahmet Ozbay

Department of Aerospace Engineering,
Iowa State University,
2271 Howe Hall, Room 1200,
Ames, IA 50011-2271

Wei Tian

Department of Aerospace Engineering,
Iowa State University,
2271 Howe Hall, Room 1200,
Ames, IA 50011-2271
e-mail: tianwei@sjtu.edu.cn

Hui Hu[1]

Department of Aerospace Engineering,
Iowa State University,
2271 Howe Hall, Room 1200,
Ames, IA 50011-2271
e-mail: huhui@iastate.edu

An experimental study was carried out to investigate the aeromechanics and wake characteristics of dual-rotor wind turbines (DRWTs) in either co-rotating or counter-rotating configuration, in comparison to those of a conventional single-rotor wind turbine (SRWT). The experiments were performed in a large-scale aerodynamic/atmospheric boundary layer (AABL) wind tunnel, available at Iowa State University with the oncoming atmospheric boundary-layer (ABL) airflows under neutral stability conditions. In addition to measuring the power output performance of DRWT and SRWT models, static and dynamic wind loads acting on those turbine models were also investigated. Furthermore, a high-resolution digital particle image velocimetry (PIV) system was used to quantify the flow characteristics in the near wakes of the DRWT and SRWT models. The detailed wake-flow measurements were correlated with the power outputs and wind-load measurement results of the wind-turbine models to elucidate the underlying physics to explore/optimize design of wind turbines for higher power yield and better durability.
[DOI: 10.1115/1.4031476]

Introduction

Wind energy, as one of the most promising renewable energy sources, has been playing an increasingly important role in the worldwide energy production portfolio in recent years. Efficient use of wind energy can provide an eco-friendly solution for energy production, thereby alleviating dependence on hydrocarbons and reducing CO_2 emissions. Because of its simplicity, reliability, and durability, horizontal axis wind-turbine (HAWT) design is the predominant design for utility-scale turbines at this time. Although HAWTs have been used widely in modern onshore and offshore wind farms, almost all of them are SRWTs. The performance of a wind turbine is usually measured in terms of the nondimensional power coefficient, C_P, which is the ratio of the energy harvested by the wind turbine to the total kinetic energy of the oncoming airflows passing through the area spanned by the turbine rotor. By applying conservation laws, a maximum limit on C_P ($\leq 59\%$) of a SRWT can be obtained, which is usually called as the Betz limit [1]. The value of 59% for the Betz limit is actually misleading, as it assumes no wake swirl or viscous losses, and an infinite number of rotor blades. When these assumptions are removed, the maximum power coefficient potential of a HAWT would be less than 0.50 [2–4]. It indicates that more than 50% of the energy available in the oncoming airflow actually escapes without being harnessed.

In recent years, a concept of a DRWT has been suggested to increase the overall power production from the oncoming airflow. For a DRWT system with two rows of rotors installed in a back-to-back configuration, the second (downwind) rotor can exploit the unharnessed energy in the wake of the upwind rotor, thereby increasing the energy harnessing capability of the wind turbine. It should be noted that, by extending the Rankine–Froude momentum theory used to compute the Betz limit to study multirotor turbines [1], Newman [5] confirmed theoretically that wind-turbine designs with multirotors can surpass the 59% Betz limit. He found that the maximum C_P for an equal-size DRWT design would be

0.64, i.e., an 8% improvement over the Betz limit, and further addition of rotor stages would give diminishing returns.

There have been a number of numerical and experimental studies, showing significant increase in the energy yield of DRWT systems, in comparison to that of SRWT systems. A prototype of a 6-kW DRWT was built in California and completed field testing in 2002 [6], and the DRWT system was found to extract 30% more power from the same oncoming wind, in comparison with a conventional SRWT design. Another field study on a 30-kW prototype DRWT also showed that the power increase of 21% over a conventional SRWT system at a rated wind speed of 10.6 m/s [7]. More recently, Habash et al. [8] conducted a wind-tunnel study with a small-scale DRWT system, and found that the DRWT system could produce up to 60% more energy than a SRWT system, and was also capable to reduce cut-in speed while maintaining turbine performance. Furthermore, Shen et al. [9] carried out a numerical study on the performance of DRWTs, and showed that DRWT systems could produce an increase about 43.5% in the annual energy production (AEP) at higher wind speeds when compared to conventional SRWT systems.

It should be noted that a counter-rotating rotor concept (i.e., the rotors rotate in opposite directions) has been widely used in marine (e.g., counter-rotating propellers used by Mark 46 torpedo) and aerospace (e.g., Soviet Ka-32 helicopter with coaxial counter-rotating rotors) applications to increase aerodynamic efficiency of the systems. For a DRWT system, the counter-rotating concept could also be implemented as the two rotors are installed very close to each other. With the two rotors in a counter-rotating configuration, the downwind rotor could benefit from the disturbed wake flow of the upwind rotor (i.e., with a significant tangential velocity component or swirling velocity component in the upwind rotor wake). As a result, the downwind rotor could harvest the additional kinetic energy associated with the swirling velocity of the wake flow.

In the present study, a comprehensive investigation was conducted to examine the aeromechanic performance and wake characteristics of DRWTs with co-rotating or counter-rotating rotors, in comparison to those of a conventional SRWT system. The experimental study was performed in a large-scale AABL wind tunnel located at the Aerospace Engineering Department of Iowa State University. Scaled DRWT and SRWT models were placed

Fig. 1 Test section of the AABL wind tunnel

in a typical ABL wind under neutral stability conditions. In addition to measuring the power outputs of the DRWT and SRWT systems, static and dynamic wind loads acting on the test models were also investigated to assess the effects of the extra (downwind) rotor in either counter-rotating (rotors rotate at opposite directions) or co-rotating (rotors rotate at same direction) configuration on the power production performance of each rotors and the overall system performance, as well as the resultant dynamic wind loads (both aerodynamic forces and bending moments) acting on the DRWT systems. Furthermore, a high-resolution PIV system was also used in the present study to quantify the transient behavior (i.e., formation, shedding, and breakdown) of unsteady wake vortices and the wake-flow characteristics behind the DRWT and SRWT models. The detailed flow field measurements were correlated with the power output data and dynamic wind-loading measurements to elucidate underlying physics for higher total power yield and better durability of wind turbines operating in turbulent ABL winds.

Experimental Setup and Procedure

AABL Wind Tunnel. The present experimental study was performed in the AABL wind tunnel located at the Aerospace Engineering Department of Iowa State University. The AABL wind tunnel, as shown in Fig. 1, is a closed-circuit wind tunnel with a test section of 20 m long, 2.4 m wide, and 2.3 m high, optically transparent side walls, and a capacity of generating a maximum wind speed of 45 m/s in the test section. Spike structures, chains, and/or arrays of wood blocks were placed on the wind-tunnel floor upstream of the test section to generate a turbulent boundary layer flow analogous to a typical ABL wind seen in wind farms. The boundary layer growth of the simulated ABL wind under zero pressure gradient condition was achieved by adjusting the ceiling profile of the test section of the wind tunnel.

As described in Zhou and Kareem [10] and Jain [11], the mean velocity profile of an ABL wind can usually be fitted well by using a power function, i.e., $U(y) = U^*_{YG}(Y/Y_G)^{\alpha}$, where U_{YG} is the wind speed at a reference (hub) height of Y_G. The value of power-law exponent, α, is associated with the terrain roughness. Figure 2 shows the measured streamwise mean velocity (normalized with the hub height velocity, U_{hub}) and turbulence intensity (the ratio of standard deviation in velocity fluctuations, σ_U, to the mean flow velocity, U) profiles of the oncoming flow in the test section for the present study. As shown in Fig. 2, the power-law exponent of the curve fitting to the measurement data was found to be $\alpha \approx 0.11$, corresponding to the offshore boundary layer wind profile according to the ISO offshore standard [11] ($\alpha \approx 1/8.4$). The measured hub height turbulence intensity being around 10%, which is in the range of the hub turbulence intensity levels measured over Horns Rev offshore wind farm as reported in Hansen et al. [12]. For comparison, typical hub height turbulence intensity for offshore wind turbines is about 8%, as described in Tong [13].

Wind-Turbine Models. The SRWT model used in the present study represents the most commonly used three-blade HAWTs seen in modern wind farms. Figure 3 shows a schematic of the SRWT model along with typical cross-section profiles of the turbine rotor blades. The model turbine has a rotor radius of 140 mm and hub height of 225 mm. With the scale ratio of 1:320, the model turbine would represent 2-MW wind turbines commonly seen in modern wind farms with a rotor diameter of about 90 m and a tower height of about 80 m. The rotor blades of the model turbine are made of a hard plastic material by using a rapid prototyping machine. The rotor blades have the same airfoil cross sections and platform profiles as ERS-100 prototype turbine blades developed by TPI Composites. As shown in Fig. 3, the rotor blade
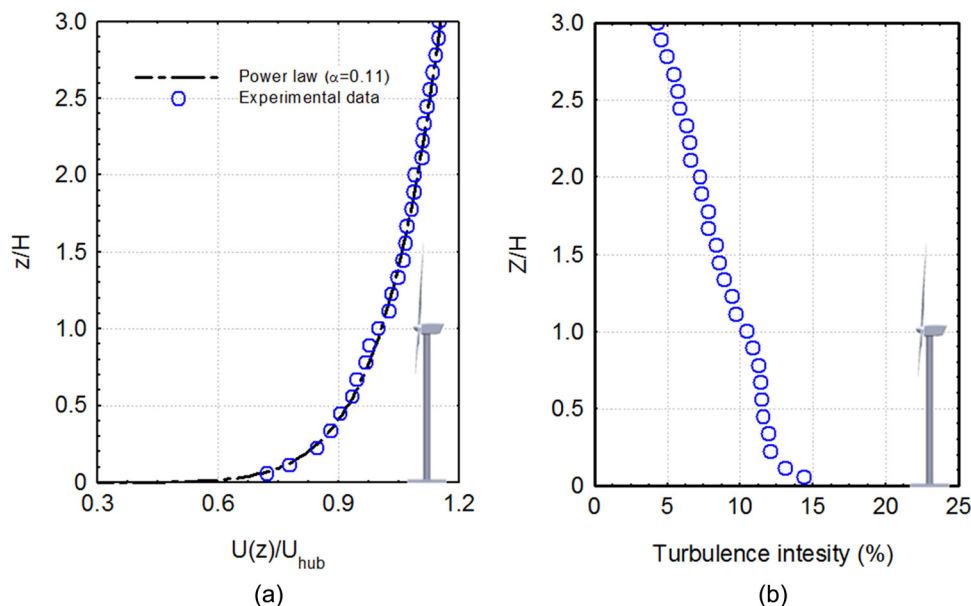

Fig. 2 Measured flow characteristics of the oncoming flow for the present study: (a) mean streamwise flow velocity and (b) turbulence intensity
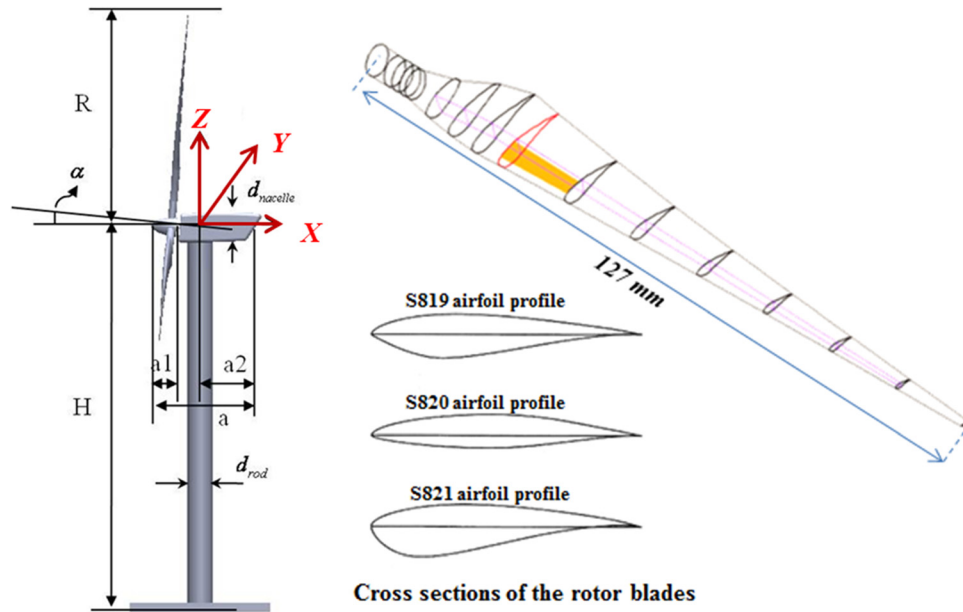
Fig. 3   Schematic of the SRWT model used in the present study

has a constant circular cross section from the blade root to 5% blade radius (R), and three NREL airfoil profiles (S819, S820, and S821) are used at different spanwise locations along the rotor blade. The S821 airfoil profile is used between $0.208R$ and $0.40R$, the S819 primary airfoil is positioned at $0.70R$, and the S820 airfoil profile is specified at $0.95R$. A spline function is used to interpolate the prescribed crosssection profiles to generate the three-dimensional model of the rotor blade using SOLIDWORKS software. In the present study, the rotor blades were mounted on a turbine hub with a pitch angle of 3.0 deg (i.e., $\theta = 3.0$ deg). A DC electricity generator (Kysan, FF-050 S-07330) was installed inside the nacelle of the model turbine, which would produce electricity as driven by the rotating blades. Further detailed information about the design parameters and manufacture of the SRWT model is available in Yuan et al. [14] and Tian et al. [15]. It should be noted that the blockage ratio of the wind-turbine models (i.e., the ratio of the turbine blade swept area to the crosssection area of the AABL tunnel) was found to be less than 2%. Thus, the blockage effects of the wind-turbine models in the test section would be almost negligible for the present study.

The DRWT models used in the present study were made by adding a second set of blades downwind to the SRWT model described above. Figure 3 shows a schematic of the DRWT models with the two rotors in either co-rotating or counter-rotating configuration. In the present study, the front rotors for the co-rotating and counter-rotating DRWT systems are identical, which were set to rotate in a counterclockwise direction as driven by the oncoming airflow. For the co-rotating DRWT model, the back rotor has the same blade design as the front rotor. Therefore, both the front and back rotors would rotate in the same direction, as driven by the oncoming airflow. For the counter-rotating DRWT model, the blades of the back rotor were made by mirroring the airfoil configurations of the front rotor. As a result, the back rotor would rotate in a clockwise direction when driven by the oncoming airflow, which is opposite to the rotational direction of the front rotor. The front and back rotors of the DRWT models were connected to two DC electricity generators (Kysan, FF-050 S-07330) inside the turbine nacelle. As a result, the front and back rotors of the DRWT models can rotate independently with different rotating speeds, corresponding to the different local wind speeds. The distance between the front and back rotors of the DRWT models was fixed at $L/D = 0.25$, where D is the rotor diameter.

During the experiments, the mean wind speed at the hub height of the model turbines was set to be 5.0 m/s (i.e., $U_{hub} = 5.0$ m/s).

The Reynolds number based on the averaged chord length of the rotor blades (C) and the incoming wind speed at the hub height (U_{hub}) was found to be about 7000 (i.e., $Re_C \approx 7000$). It should be noted that this Reynolds number is significantly lower than those of large-scale wind turbines in the field, i.e., $Re_C \approx 7.0 \times 10^3$ for the present study versus $Re_C > 1.0 \times 10^6$ for the large-scale wind turbines [16]. According to Alfredsson et al. [17], whereas the Reynolds number of a wind turbine may have a significant effect on the power production performance of the wind turbine (i.e., the maximum power coefficient would be much lower for a small-scale model turbine operating at a lower Reynolds number), the wake characteristics and the evolution of the unsteady vortices in the turbine wake would become almost independent of the Reynolds number when the Reynolds number of the model turbine is sufficiently high. Instead of using a chord Reynolds number, the Reynolds number based on the turbine rotor diameter (D) and the flow velocity at the turbine hub height (U_{hub}), i.e., Re_D, was also used to characterize the wake measurement results [18]. Chamorro et al. [18] found that fundamental flow statistics (i.e., normalized profiles of mean velocity, turbulence intensity, kinematic shear stress, and velocity skewness) in the turbine wake have asymptotic behavior with the Reynolds number. Mean velocity in the turbine wake was found to reach Reynolds-number independence at a lower value compared to that of higher-order statistics (i.e., turbulence intensity, turbulent kinematic energy, and Reynolds shear stress). Reynolds-number independence for mean velocity could be reached at $Re_D \approx 4.8 \times 10^4$, and that of higher-order statistics started at $Re_D \approx 9.3 \times 10^4$. It should be noted that the Reynolds number based on the rotor diameter of the turbine and the wind speed at the turbine hub height for the present study is about 90,000 (i.e., $Re_D \approx 9.0 \times 10^4$), which is in the range of the required minimum Reynolds number as suggested by Chamorro et al. [18] to achieve Reynolds-number independence of the turbine wake statistics.

Measurement Systems Used in the Present Study

Power-Output Measurements. In the present study, the rotation speed of the turbine rotors was adjusted by applying different electric loads to the small DC electricity generators installed inside the turbine nacelles. The turbine rotation speed Ω can change from 0 to 2200 rpm, and the tip-speed ratio ($\lambda = \Omega R/U_{hub}$, where R is the radius of the rotor) of the turbine models is in the range from 0 to 6.5. The power outputs of the turbine models

were achieved by measuring the voltage outputs of the small generators installed in the turbine nacelles and the corresponding electrical loadings applied to the electric circuits. During the experiments, the voltage outputs of each generator were acquired through an A/D board plugged into a host computer at a data-sampling rate of 1.0 kHz for 120 s. By applying different electric loads to the small electricity generators, the optimum tip-speed-ratio of a turbine model, i.e., at the tip-speed ratio when the turbine model reaches the maximum power output, can be determined. The optimum tip-speed ratio of the SRWT model used in the present study was found to be $\lambda \approx 5.0$. For comparison, a typical three-blade HAWT on a modern wind farm usually has a tip-speed ratio of $\lambda \approx 4.0$–8.0, as described in Hu et al. [19]. During the experiment, the front and back rotors of DRWT systems were set to operate at their own optimum tip-speed ratios, which was $\lambda \approx 4.6$ and $\lambda \approx 4.0$ for the front and back rotors, respectively.

Wind-Loading Measurements. For the wind-turbine models used in the present study, aluminum rods were used as the turbine towers to support the turbine nacelles and the rotor blades. Through holes in the wind-tunnel floor, the aluminum rods were connected to high-sensitivity force-moment sensors (JR3, Model 30E12A-I40) to measure the wind loads (aerodynamic forces and bending moments) acting on the wind-turbine models. The JR3 force-moment sensor is capable of providing time-resolved measurements of all three components of the aerodynamic forces and the moment (torque) about each axis. The precision level of the force-moment sensor cell for force measurements is ±0.25% of the full range (40 N). During the experiments, the wind-load data were acquired at a sampling rate of 1000 Hz with a duration of 300 s for each test case. A Monarch Instrument Tachometer was also used to measure the rotation speed of the wind-turbine blades independently.

PIV Measurements. In addition to the power output and wind-loading measurements, a high-resolution PIV system was also used in the present study to conduct detailed flow field measurements in the vertical plane passing through the symmetrical plane of the turbine models to characterize the flow characteristics of the turbine wakes. Figure 4 shows the schematic of the experimental setup for PIV measurements. For the PIV measurements, the incoming airflow was seeded with ~1 μm oil droplets by using a droplet generator. Illumination was provided by a double-pulsed laser adjusted on the second harmonic and emitting two pulses of 200 mJ at the wavelength of 532 nm. The thickness of the laser sheet in the measurement region was about 1.0 mm. To have a
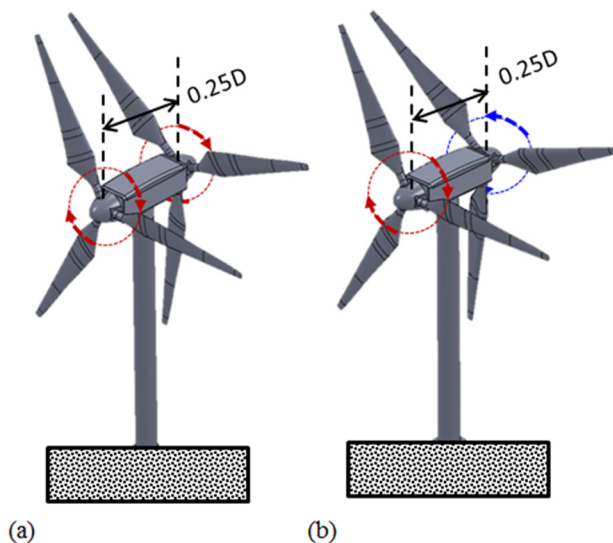

Fig. 4 Schematic of the DRWT models used in the present study: (*a*) co-rotating DRWT and (*b*) counter-rotating DRWT

larger measurement window along the streamwise direction to reveal the evolution of the unsteady wake vortex and turbulent flow structures behind the model turbine, two high-resolution 12-bit CCD cameras (PCO1600, CookeCorp) were used for PIV image acquisition with the axis of the cameras perpendicular to the laser sheet. The CCD cameras and the double-pulsed Nd:YAG lasers were connected to a workstation (host computer) via a digital delay generator (Berkeley Nucleonics, Model 565), which controlled the timing of the laser illumination and the image acquisition.

After PIV image acquisition, instantaneous PIV velocity vectors were obtained by a frame to frame cross-correlation techniques involving successive frames of patterns of particle images in an interrogation window of 32×32 pixels. An effective overlap of 50% of the interrogation windows was employed in PIV image processing. After the instantaneous velocity vectors (u_i, v_i) were determined, the vorticity (ω_z) can be derived. The distributions of the ensemble-averaged flow quantities such as the mean velocity, normalized Reynolds stress ($\bar{\tau} = -\overline{u'v'}/U_{hub}^2$), and in-plane turbulence kinetic energy (TKE = $0.5 * (\overline{u'^2} + \overline{v'^2})/U_{hub}^2$) were obtained from a cinema sequence of about 1000 frames of instantaneous PIV measurements. The measurement uncertainty level for the velocity vectors is estimated to be within 2%, whereas the uncertainties for the measurements of ensemble-averaged flow quantities such as Reynolds stress and turbulent kinetic energy distributions about 5%.

In the present study, both "free-run" and "phase-locked" PIV measurements were performed during the experiments. The free-run PIV measurements were conducted to determine the ensemble-averaged flow statistics (e.g., mean velocity, Reynolds stress, and turbulence kinetic energy) of the turbine wakes. For the free-run PIV measurements, the image-acquisition rate was preselected at a frequency that is not a harmonic frequency of the rotating frequency of the turbine rotor blades to ensure physically meaningful measurements of the ensemble-averaged flow quantities. Phase-locked PIV measurements were conducted to elucidate more details about the evolution of unsteady wake vortices in relation to the position of the rotating rotor blades. For the phase-locked PIV measurements, a digital tachometer was used to detect the position of a premarked rotor blade. The tachometer would generate a pulsed signal as the premarked rotor blade passed through the vertical PIV measurement plane. The pulsed signal was then used as the input signal to a digital delay generator (DDG) to trigger the digital PIV system to achieve the phase-locked PIV measurements. By adding different time delays between the input signal from the tachometer and the TTL signal output from the DDG to trigger the digital PIV system, the phase-locked PIV measurements at different rotation phase angles of the premarked rotor blade can be accomplished. At each preselected phase angle (i.e., corresponding to different positions of the premarked rotor blade related to the vertical PIV measurement plane), 400 frames of instantaneous PIV measurements were used to calculate the phase-averaged velocity, vorticity (w_z), and swirling strength (λ_{ci}) distributions in the wake flows behind the turbine models (Fig. 5).

Time-Resolved Measurements With a Cobra Anemometry Probe. In the present study, a Cobra Anemometry Probe (TFI Series 100 of Turbulent Flow Instrumentation) was also used to provide time-resolved flow velocity measurement data at the points of interest to supplement the PIV measurements. The Cobra Anemometry Probe is capable of measuring all three components of instantaneous flow velocity vector at a prescribed point with a sampling rate of up to 2.5 kHz. Other flow quantities, such as the turbulence intensity, Reynolds stresses, turbulence kinetic energy, and other higher order terms of the flow statistics can also be derived based on the measurement results of the Cobra Anemometry Probe. During the experiments, the Cobra Anemometry Probe was used to acquire measurement data at a data sampling rate of 2.5 kHz for 30 s at each measurement point.
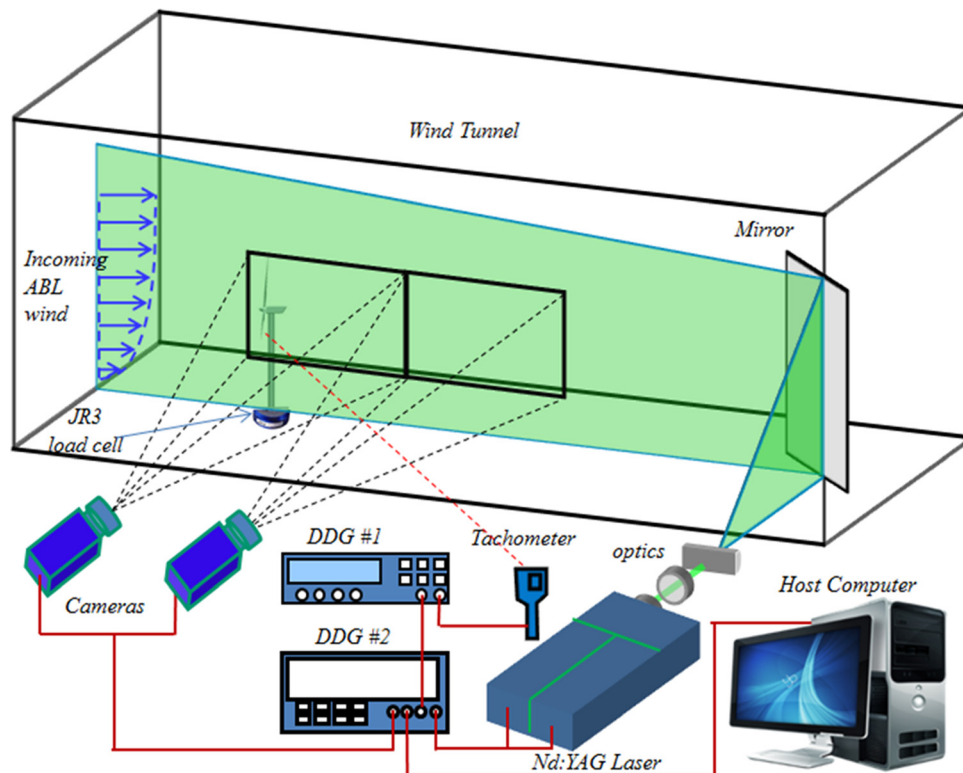
Fig. 5   Experimental setup used for PIV measurements

Experimental Results and Discussion

Power Output Measurements. Figure 6 gives the variations of the measured power outputs of the co-rotation and counter-rotating DRWT models as a function of the electric loads applied to the electric circuits associated with generators driven by the front and back rotors of the DRWT systems. The power output data of the SRWT model is also presented in the plot as the comparison baseline. It should be noted that all the power output data given in Fig. 6 were normalized with the maximum power output of the SRWT system operating at the optimum tip-speed ratio $\lambda \approx 5.0$ with the applied electric loading being about 28.2 Ω.

As shown in Fig. 6, the power outputs of the DRWT models (i.e., the sum of the power outputs from the front and back rotors) were found to be greater than that of the SRWT model. It indicates that, because of the addition of the second rotors, the DRWT

Fig. 6   Variations of the normalized power outputs of the turbine models as a function of the applied electric load

systems can extract more wind energy from the same oncoming airflow, in comparison to the SRWT system. More specifically, regardless of the rotational direction of the back rotors, the DRWT models used in the present study were found to generate at least 40% more power than the SRWT model within the entire range of the applied electrical loading. When the rotation direction of the back rotor is taken into account, whereas the co-rotating DRWT model could generate up to 48% more power than the SRWT model, the counter-rotating DRWT model was found to be able to harvest up to 60% more wind energy from the same oncoming ABL wind, in comparison to the SRWT model. The measurement results highlighted the advantage of the DRWT systems over conventional SRWT system in wind-power generation. This advantage was found to be enhanced with the counter-rotating DRWT design.

It should also be noted that, although DRWT systems operate with two rotors, the gain in power generation over a conventional SRWT system was found to be far less than 100%. It indicates that, even though two rotors were used, DRWT systems are still far from being able to generate twice as much wind power as a conventional SRWT system. As described shown schematically in Fig. 4, the distance between the front and back rotors for the DRWT models used in the present study was set to $L/D = 0.25$, where D is rotor diameter. The significant power loss (more than 40%) was believed to be mainly because of the rotor-to-rotor interactions between the front and back rotors for the DRWT systems.

The rotor-to-rotor interferences were also revealed quantitatively from normalized power output data given in Fig. 6. For the DRWT systems, the presence of the downwind rotors (i.e., the back rotors) was found to affect the power output of the upwind rotors (i.e., the front rotors) substantially. With the same rotor blades being used as the front rotors of the DRWT models and the rotor of the SRWT model, because of the existence of the back rotors, the upwind rotors of the DRWT models were found to harvest about 11% less energy from the same oncoming airflow, in comparison to the SRWT rotor (i.e., without the existence of a
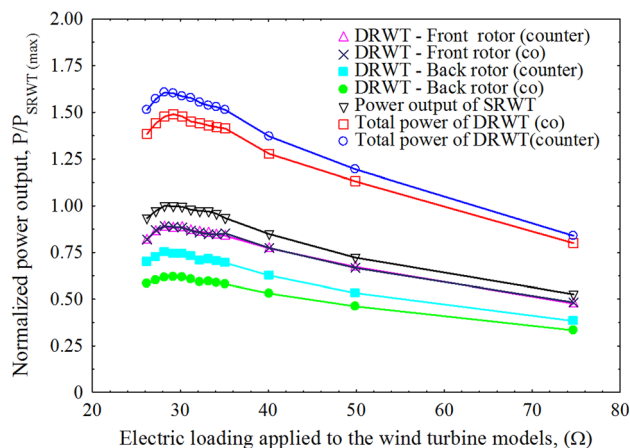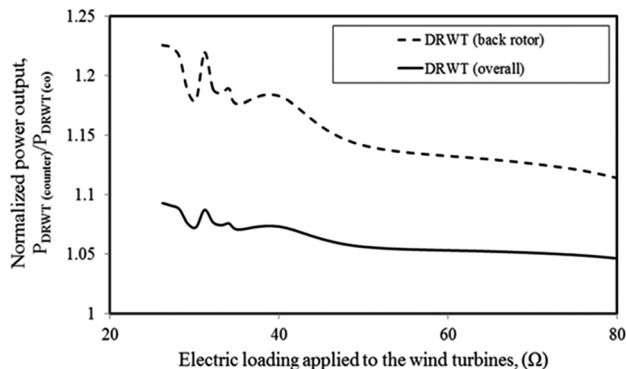
Fig. 7 Ratios of the downwind (back) rotor and overall power outputs of the counter-rotating DRWT model to those of the co-rotating DRWT model

back rotor in the near wake). The power losses of the upwind rotors were found to be almost the same for the DRWT models in either co-rotating or counter-rotating configuration. It indicates that the power losses of the front rotors are almost independent of the rotational directions of the downwind rotors for the DRWT systems.

Because the downwind rotors (i.e., the back rotors) are located in the near wakes of the upwind rotors for the DRWT systems, the back rotors were found to be much vulnerable to the severe power losses associated with the velocity deficits in near wakes of the upstream rotors. Corresponding to the close spacing between the two rotors (i.e., $L/D = 0.25$) for the DRWT models used in the present study, significant power losses of the back rotors can be observed from the measurement data given in Fig. 6. Because of the rotor-to-rotor interactions between the front and back rotors, the power loss for the downwind rotor of the co-rotating DRWT model was found to be as high as 40%, in comparison to the power generation capacity of the rotor of the SRWT model (i.e., the case without the existence of the upwind rotor). The power

loss of the downwind rotor for the counter-rotating DRWT model was found to be about 25% at the same test conditions.

Figure 7 shows the ratios of the measured power outputs of the downwind rotor (i.e., back rotor) and the overall power outputs of the counter-rotating DRWT model to those of the co-rotating DRWT model as a function of the electric loading applied to the wind turbines, which can be used to reveal the effects of the rotational direction of the downwind (back) rotors on the power production performances of the DRWT systems more clearly and quantitatively. Although the upwind rotors (i.e., the front rotors) of the DRWT models were found to have almost the same power outputs regardless the rotational direction of the downwind rotors, the downwind rotor in counter-rotating configuration was found to be able to harvest up to 23% more wind energy from the same oncoming airflow, in comparison to the case with the downwind rotor in co-rotating configuration. As a result, the counter-rotating DRWT model was found to generate up to 9% more power than the co-rotating DRWT model when mounted in the same oncoming ABL wind.

As described above, because the upwind rotors (i.e., the front rotors) of the DRWT models in either co-rotating or counter-rotating configuration were found to have almost the same power outputs, the higher power output of the counter-rotating DRWT model was found to be mainly contributed by the counter-rotating back rotor. As described above, the idea behind the counter-rotating DRWT concept is to take advantage of the significant swirling velocity (i.e., tangential or azimuthal velocity component) in the near wake of the upstream rotor. As described in Yuan et al. [14], when the swirling velocity induced by the upwind rotor is in the same rotation direction as the downwind rotor, the swirling velocity in the wake flow would result in additional torque acting on the downwind rotor blades to drive the rotor.

From the energy conversion point of view, when rotating at an opposite direction to the upstream rotor, the downwind rotor installed in the near wake of the upwind rotor could harness the additional kinetic energy associated with the swirling velocity induced by the upwind rotor. Figure 8 presents the measured
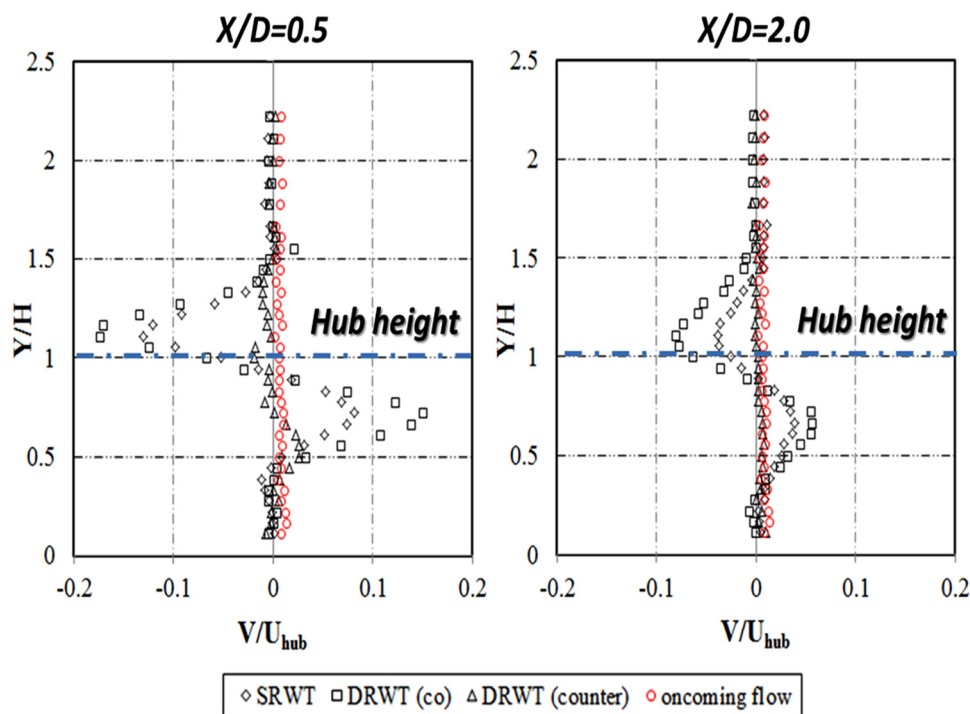

Fig. 8 Measured azimuthal (swirling) velocity profiles in the wake flows behind the SRWT and DRWT models at the downstream location of $X/D = 0.5$ and $X/D = 2.0$

azimuthal (swirling) velocity profiles in the wake flows behind the SRWT and DRWT models at the downstream location of $X/D = 0.5$ and $X/D = 2.0$. Although the azimuthal (swirling) velocity in the wake flow behind the counter-rotating DRWT model was always very small (i.e., similar to the oncoming airflow), the magnitudes of the azimuthal (swirling) velocity in the wake flows behind the co-rotating DRWT and SRWT models were found to be significant. Similar as those described in Yuan et al. [14], the significant difference in the evolution characteristics of the azimuthal (swirling) velocity can be used to explain why the counter-rotating DRWT model has a better power production performance compared with the co-rotating DRWT model. As shown in Fig. 8, the back rotor of the co-rotating DRWT model would amplify the azimuthal (swirling) velocity in the wake flow, the kinetic energy associated with the azimuthal (swirling) velocity would escape without being harnessed. Because the additional kinetic energy associated with the azimuthal (swirling) velocity in the wake of the front rotor were harvested by the back rotor of the counter-rotating DRWT model, the (swirling) velocity was found to become almost negligible in the wake flow behind the counter-rotating DRWT model. It can also be observed that the (swirling) velocity in the wake flows behind the SRWT and co-rotating DRWT model would decay gradually as the downstream distance increases and vanish eventually further downstream.

Wind-Loading Measurement Results. As described above, the JR3 force-moment sensor used in the present study can provide time-resolved measurements of all three components of the aerodynamic forces and the moment (torque) about each axis. Although similar features were also revealed by the other components of the aerodynamic forces and the moments, only the measured thrust coefficient, C_{Fx}, and the corresponding bending moment coefficient, C_{Mz}, were presented here to reveal the characteristics of the wind loads acting on the DRWT models, in comparison to those acting on the SRWT model. In the present study, the thrust coefficient, C_{Fx}, and bending moment coefficient, C_{Mz}, were defined as $C_{Fx} = F_x / (0.5\rho U_{hub}^2 \pi R^2)$ and $C_{Mz} = M_z / (0.5\rho U_{hub}^2 \pi R^2 H)$, respectively, where ρ is the density of air, R is the radius of the wind-turbine rotor, and U_{hub} is the mean flow velocity at the hub height H.

Based on the time sequences of the wind-load measurement data acquired at a sampling rate of 1000 Hz in a duration of 300 s, both the mean values and standard deviations of the dynamic wind loads acting on the wind-turbine models can be determined. Table 1 lists the mean (static) wind loads acting on the SRWT and DRWT models in the terms of the thrust and bending moment coefficients of the turbine models when the turbine models were mounted in the same oncoming ABL wind. The mean wind-load measurement data were found to correlate well with the power output readings of the turbine models given in Fig. 6. Although the addition of the second rotors (i.e., back rotors) would increase the total power outputs of the DRWT models up to 60% as shown in Fig. 6, it was also found to cause about 60% more wind loads acting on the DRWT models, in comparison to those of the conventional SRWT model. The higher mean wind loads acting on the DRWT systems would necessitate stronger towers and foundations to support the DRWT systems. It should also be noted that, in addition to the higher mean wind loads, the tower of a DRWT

system would also have to stand additional weights of the second rotor and the additional powertrain system associated with the second rotor as well as other extra components in the much bigger nacelle. All of these would cause higher initial capital costs to build DRWT systems, in comparison to the conventional SRWT systems. From the comparisons of the mean wind-load data of the two DRWT models used in the present study, it can also be seen that, although the counter-rotating DRWT model would generate up to 9% more power than the co-rotating DRWT model as described above, the mean wind loads acting on the counter-rotating DRWT model were found to be only slightly higher (i.e., only about 2% higher) than those acting on the co-rotating DRWT model.

Table 2 presents the standard deviations of the dynamic wind loads acting on the SRWT and DRWT models when they were mounted in the same oncoming ABL wind. It should be noted that larger fluctuation amplitudes of the dynamic wind loads acting on a wind turbine would indicate more severe fatigue loads acting on the wind turbine, which would affect the durability and lifetime of the wind turbine. The measurement data listed in Table 2 reveal that the fluctuating amplitudes of the dynamic wind loads (i.e., both the standard deviations of the thrust and corresponding bending moment) acting on the DRWT models were found to be about 17–25% greater than those acting on the SRWT model. The higher fluctuating amplitudes of the dynamic wind loads acting on the DRWT models were believed to be closely related to the complex interactions between the front and back rotors. As described above, because the back rotors operate in the wakes of the front rotors for the DRWT systems, the dynamic wind loads acting on the back rotors are expected to fluctuate much more significantly because of the much higher turbulence intensity levels in the wakes of the front rotors. The higher fluctuating amplitudes of the dynamic wind loads would cause much greater fatigue wind loads acting on the back rotors, resulting in a reduced fatigue lifetime for the downwind rotors. The dynamic wind-load data given in Table 2 also reveal that the fluctuation amplitudes of the dynamic wind loads acting on the counter-rotating DRWT model were found to be slightly higher (∼5%) than those acting on the co-rotating DRWT model.

Wake-Flow Characteristics Behind the SRWT and DRWT Models. As described in Hu et al. [19], the wake flow behind a wind turbine sited in turbulent ABL wind is very complicated, particularly in the near wake close to the turbine rotor (i.e., in the near region of $X/D < 1.0$). The characteristics of the near wake flow are affected greatly by the presence of the rotor (i.e., the number of blades, blade aerodynamics, such as attached or stalled flows, 3D effects, and tip vortices) and the interactions among the turbine rotors, towers and nacelles [20]. Because the rotor blades of the turbine are driven by the oncoming airflow to convert a portion of the kinetic energy of the oncoming airflow into electric energy (via electricity generator and power train sited inside the turbine nacelle), it causes the deceleration of the airflow streams as they pass through the rotation disk of the turbine rotor. Some of the oncoming airflow streams are blocked by the nonrotating components of the wind turbine, such as tower, nacelle, and hub to cause periodic shedding of the unsteady vortex structures and formation of recirculation regions and reverse flows in the wake flow. As described in Chamorro and Porte-Agel [21], the

Table 1 Comparison of the mean wind loads acting on the SRWT and DWRT models

Test wind-turbine models	Thrust coefficient (C_{Fx})	Bending moment coefficient (C_{Mz})
SRWT	0.45	0.52
DRWT (co)	0.70	0.82
DRWT (counter)	0.71	0.83

Table 2 Comparison of the standard deviation of dynamic wind loads acting on the SRWT and DWRT models

Systems	$\sigma(C_{Fx})$	$\sigma(C_{Mz})$
SRWT	0.17	0.16
DRWT (co)	0.20	0.19
DRWT (counter)	0.21	0.20

nonuniformity in both mean wind speed and turbulence intensity levels of the oncoming ABL winds, the presence of the ground as well as the complex terrain topology would also add more complex features to the turbulent wake flow behind the wind turbine.

As described above, a high-resolution PIV system was used to quantify the flow characteristics of the wakes behind the SRWT and DRWT models. Based on a cinema sequence of about 1000 frames of instantaneous PIV measurements, the ensemble-averaged flow quantities in the turbine wake flows, such as the mean velocity, normalized Reynolds stress and in-plane turbulence kinetic energy (TKE), were determined. Figure 9 gives the ensemble-averaged PIV measurements in terms of the mean velocity distributions, U/U_{hub}, and the corresponding velocity deficit, $\Delta U/U_{\text{hub}}$, in the wakes behind the wind-turbine models, where $\Delta U = U - U_{\text{freestream}}$. As shown in the PIV measurement results, because a portion of the kinetic energy carried by the oncoming airflow was harvested by the model wind turbines, the oncoming airflow streams were found to decelerate greatly as they passed through the rotation disks of the turbine blades. As a result,

significant velocity deficits were found to exist in the wakes behind the turbine models. As expected, in comparison to those behind the SRWT model, the velocity deficits in the wakes of the DRWT models were found to be much more significant, which can be attributed to the existence of the additional downwind rotors. Because the DRWT systems can harness more energy from the same oncoming airflow, thereby producing much larger velocity deficits in the wake flows. It can also be seen that, because the counter-rotating DRWT model could generate about 10% more power from the same oncoming airflow in comparison to the co-rotating DRWT system, it causes the highest velocity deficits in the wake-flow amount among the three compared wind-turbine models.

The PIV results given in Fig. 9 also reveal the existence of regions with relatively high velocity right above the turbine nacelles and within the inner roots of the turbine rotors (i.e., $Y/D < 0.1$), which extends up to $X/D = 0.5$ downstream. This is believed to be because of the aerodynamically poor design of the rotor blades at the roots (i.e., inner 25% of the rotor blades are
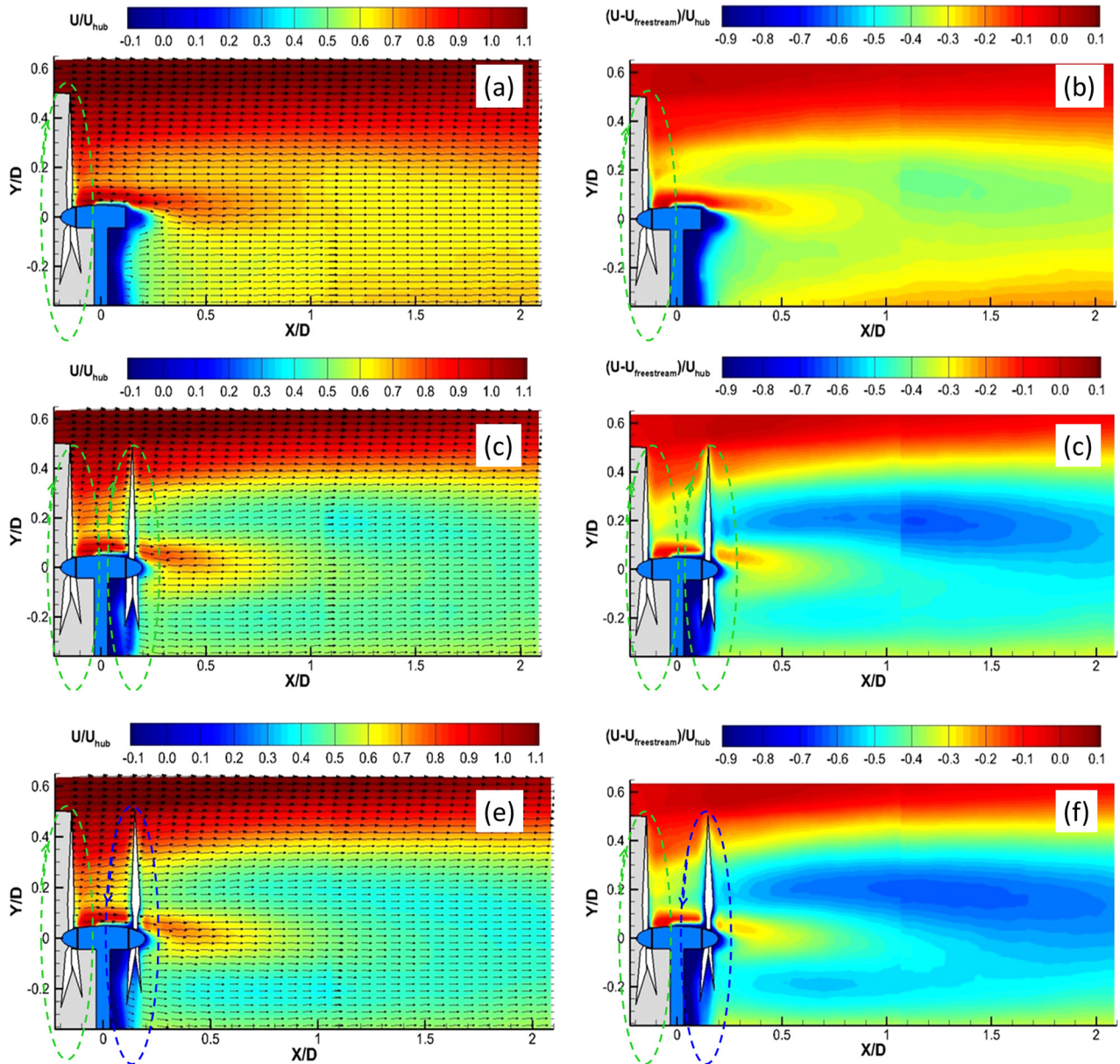

Fig. 9 Ensemble-averaged velocity, U/U_{hub}, and velocity deficit, $\Delta U/U_{\text{hub}}$, distributions in the wakes behind the SRWT and DRWT models: (a) U/U_{hub}, SRWT, (b) $\Delta U/U_{\text{hub}}$, SRWT, (c) U/U_{hub}, co-rotating DRWT, (d) $\Delta U/U_{\text{hub}}$, co-rotating DRWT, (e) U/U_{hub}, counter-rotating DRWT, and (f) $\Delta U/U_{\text{hub}}$, counter-rotating DRWT

designed mainly to provide structural integrity, instead of harvesting wind energy). It would result in a zone near the roots of turbine rotor blades, where virtually no wind energy is extracted from the oncoming airflow. A sudden drop in the streamwise velocity distributions (more pronounced in wakes behind the DRWT systems) can also observed starting from the mid-span sections of the turbine rotors, because of the high-energy harvesting rates for the segments of the turbine rotor blades. The zones with high-velocity deficits were found to move more toward the hub height as the downstream distance increases.

As described in Vermeer et al. [20], because turbulence decay rate would be much slower than the mean streamwise velocity recovery rate, it is highly desirable to characterize the turbulence characteristics (e.g., TKE and Reynold stress levels and distribution patterns) of the wake flows behind wind turbines to provide better operation conditions and longer lifetimes for the wind turbines operating turbulent ABL winds. It is well known that TKE level in a turbulent flow can usually be used as a parameter to indicate the extent of turbulent mixing in the flow. A higher TKE level in a turbine wake would indicate much more intensive mixing in the wake flow, corresponding to a much faster recovery of the velocity deficits in the turbine wake.

As suggested by Meyers and Meneveau [22], turbulent fluxes produced because of wake-induced turbulence in a turbine wake would play a very important role on the entrainment of energy from the high-speed airflow above to re-charge the wake flow behind the wind turbine. Figure 10 given the wake-induced TKE distributions in the turbine wakes, which can be used to reveal the turbulence characteristics of the wake flows behind the DRWT models, in comparison to those of the SRWT model. The wake-induced TKE distributions in the turbine wake were obtained by subtracting the TKE levels of the oncoming airflow from those of the measured TKE values in the turbine wakes (i.e., $\Delta \mathrm{TKE} = \Delta \mathrm{TKE}_{\mathrm{wake\ flow}} - \Delta \mathrm{TKE}_{\mathrm{freestream}}$). As shown in Fig. 9, although the distribution pattern of the wake-induced TKE in the turbine wake was found to be quite similar for both DRWT and SRWT cases, the absolute values of the wake-induced TKE in the turbine wakes behind the DRWT models were found to be much greater than those of the SRWT case. The regions with quite high wake-induced TKE levels were found to concentrate in the wake immediately behind the nacelle and tower of the wind-turbine models, which is believed to be closely related to the formation and shedding of unsteady wake vortices from the turbine nacelle and tower. The wake-induced TKE levels were also found to be quite high at the upper region behind the rotation disk of the turbine blades, which is correlated well to the shedding paths of the unsteady tip and root vortices from the rotating rotor blades in the PIV measurement plane. The expansion of the turbine wake with the increasing downstream distance away from the turbine rotor disk can also be observed in the wake-induced TKE distributions.

Zhou et al. [23] suggested that wake vortex instability and its breakdown would play an important role on TKE production in a turbine wake. It is evident from the measurement results shown in Fig. 10 that the onsets of the wake instabilities (i.e., the starting points of the regions with much higher wake-induced TKE levels) in the wake flows behind the wind turbines are quite different for the DRWT and SRWT systems. For the DRWT systems, the wake instabilities at the top tip level were found to take place much earlier than those of the SRWT case. It is also clear that the wake-induced TKE levels in the near region (i.e., before $X/D = 0.50$) at the tip-top height are relatively lower, where strong tip vortices were observed in the phase-locked PIV measurement results to be discussed later. The measurement results were found to agree well with the findings of Whale [24], who suggested that the near wake-tip vortices would act as a shield preventing the turbulent mixing and TKE production in the near wake of a wind turbine.

An obvious pattern change can also be observed in the wake-induced TKE distributions at the hub height level, with respect to those at the top tip level of the turbine models. Although the values of the wake-induced TKE at the turbine top tip level were found to increase rapidly with the increasing downstream distance, the wake-induced TKE values were found to increase gradually as the downstream distance increases. The values of the wake-induced TKE were found to become even negative at further
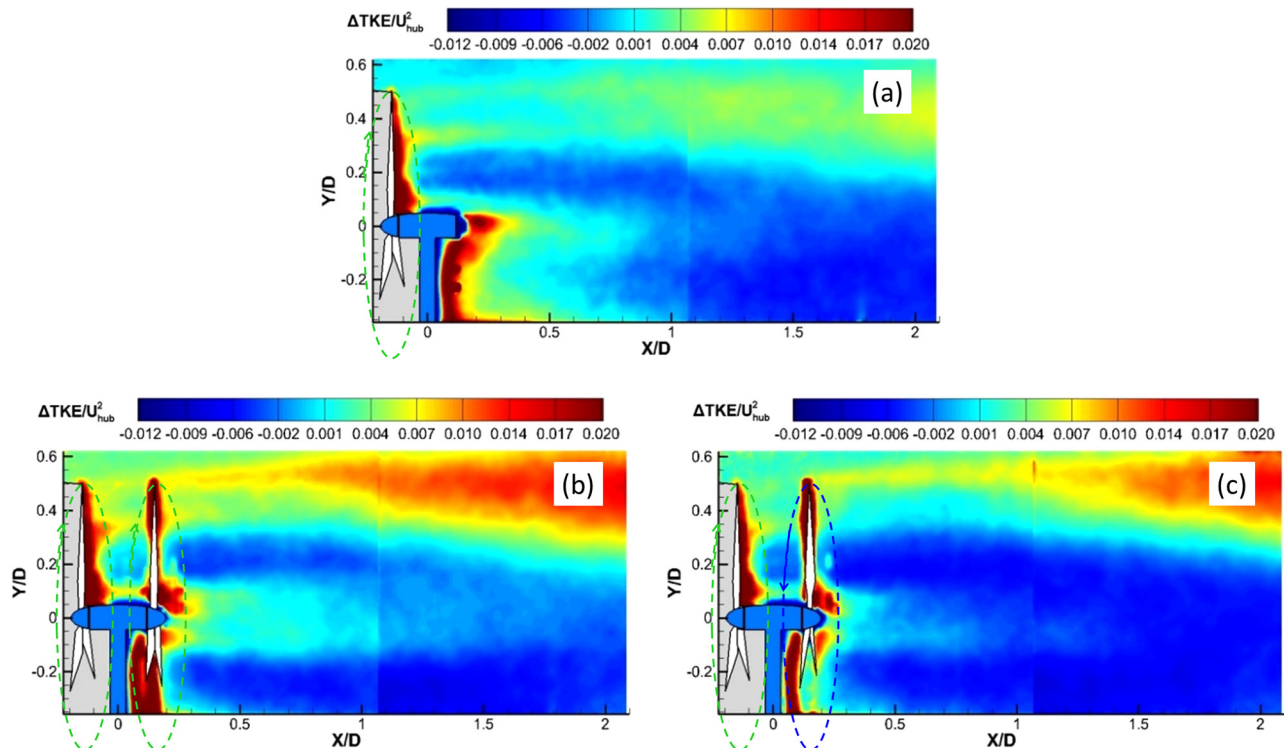

Fig. 10 Wake-induced TKE distributions ($\Delta \mathrm{TKE}/U_{\mathrm{hub}}^2$) in the wakes behind the SRWT and DRWT models: (*a*) SRWT, (*b*) co-rotating DRWT, and (*c*) counter-rotating DRWT

downstream locations, indicating that the wake flow at the turbine hub height level may be actually less turbulent than the oncoming boundary-layer airflow. Such observations were also reported by Chamorro and Porte-Agel [21] and Sherry et al. [25]. It should also be noted that the counter-rotating DRWT model was found to have the lowest wake-induced TKE values in the near wake region at the hub height among the three compared wind-turbine models.

Figure 11 presents the distributions of the normalized Reynolds shear stress, R_{uv}/U_{hub}^2, in the wake flows behind the three compared wind-turbine model. As described in Sherry et al. [25], a higher Reynolds stress level in a turbine wake would play an important role in promoting the vertical transport of the kinetic energy in the turbine wake, which will draw down more high-velocity airflow from above to the wake flow behind the wind turbine. As shown in Fig. 11, the distribution features of the Reynolds stress in the turbine wakes for the three compared turbine model were found to be quite similar. The regions with relatively higher (positive) levels of Reynolds shear stress were found to exist in the wakes at the top tips of turbine rotors, analogous to the wake-induced TKE distributions given in Fig. 10. The values of the Reynolds shear stress were found to increase rapidly in the wake flows at the top tip levels, as the downwind distance increases. Higher levels of Reynolds shear stress were also observed in the wake flows behind the turbine tower, nacelle, and root sections of the turbine rotors. It should also be noted that, although the distribution features of the Reynolds stress in the turbine wakes for the three compared turbine model were found to be quite similar, the absolute values of the Reynolds shear stress in the turbine wake behind the DRWT models were found to be almost three times as high as those of the SRWT case. In addition, the expansion of the regions with high Reynolds stress values at the upper portion of the turbine wake was also found to be much more aggressive in the wakes behind the DRWT models, in comparison with the SRWT case.

Based on the comparisons of the wake-induced TKE and Reynolds stress distributions described above, it can be suggested that, because of the additional of the second rotors (i.e., the back rotors), the wake-induced TKE and Reynolds shear stress levels in the wakes behind the DRWT models would become much higher than those of the SRWT case, which would promote a faster vertical transport of kinetic energy by entraining more high-speed airflow from above to re-charge the wakes flow behind the DRWT models. As a result, the velocity deficits in the wakes behind the DRWT models would recover much faster than that of the SRWT case.

Phase-Locked PIV Measurement Results. As described above, phase-locked PIV measurements were carried out in the present study to provide "frozen" images of unsteady wake vortex structures at different phase angles. The phase angle is defined as the angle between the vertical PIV measurement plane and the position of a premarked turbine rotor blade. The premarked rotor blade would be in the most upward position (i.e., within the vertical PIV measurement plane) at the phase angle of $\phi = 0.0$ deg. As the phase angle increases, the turbine blade would rotate out of the vertical PIV measurement plane. Figure 12 to Fig. 14 present the phase-locked PIV measurement results in the terms of the normalized streamwise velocity deficit (left), vorticity (middle), and swirling strength (right) distributions in the wakes behind the SRWT and co- and counter-rotating DRWT models at the phase angle of $\phi = 0.0$ deg, 30.0 deg, 60.0 deg, and 90.0 deg, respectively. It should be noted that, for the DRWT systems, the upwind rotor was phase-locked, whereas the downwind rotor was rotating freely (free-run) during the PIV measurements.

The phased-locked streamwise velocity deficit distributions reveal clearly the existence of large zones with relatively bigger velocity deficits in the near wakes behind the wind-turbine models. Corresponding to the better wind-energy capacity of the DRWT systems in comparison to the SRWT model, the zones
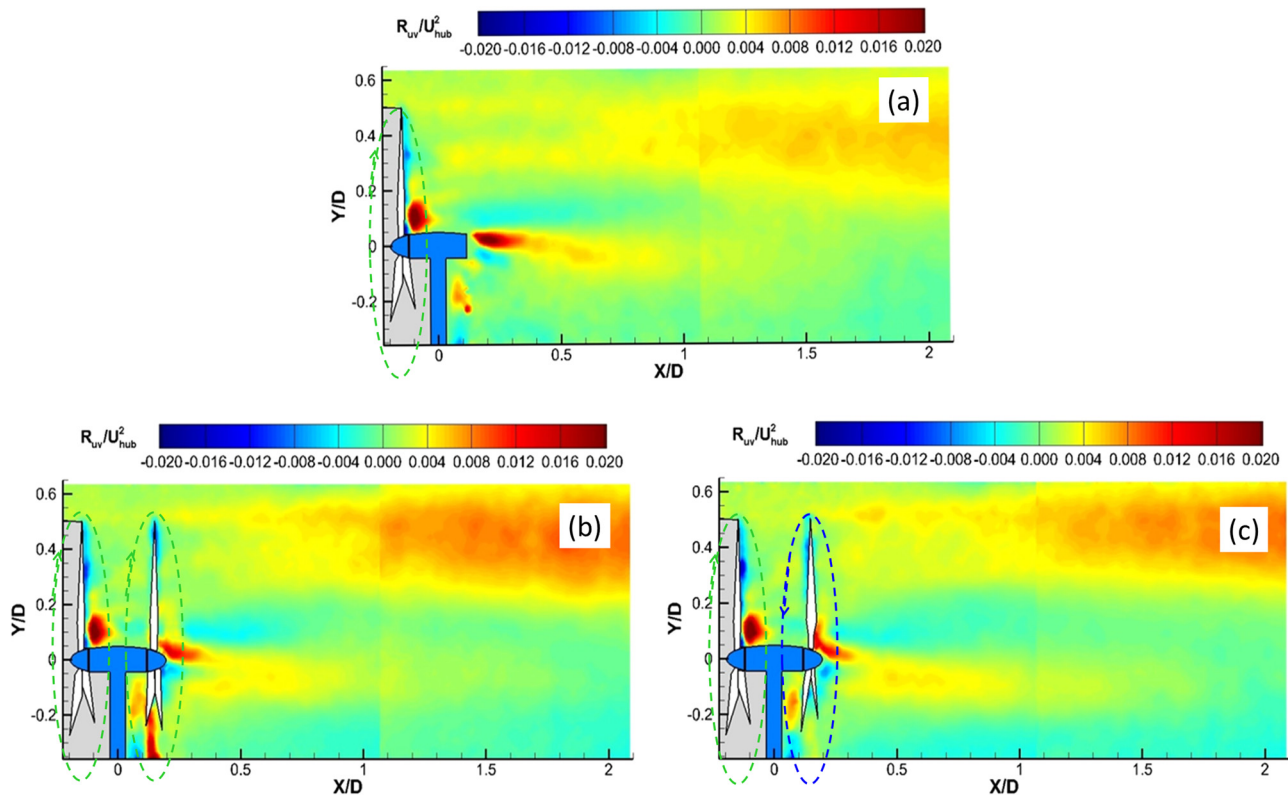

Fig. 11 Reynolds shear stress, R_{uv}/U_{hub}^2, distributions in the wakes behind the SRWT and DRWT models: (a) SRWT, (b) co-rotating DRWT, and (c) counter-rotating DRWT
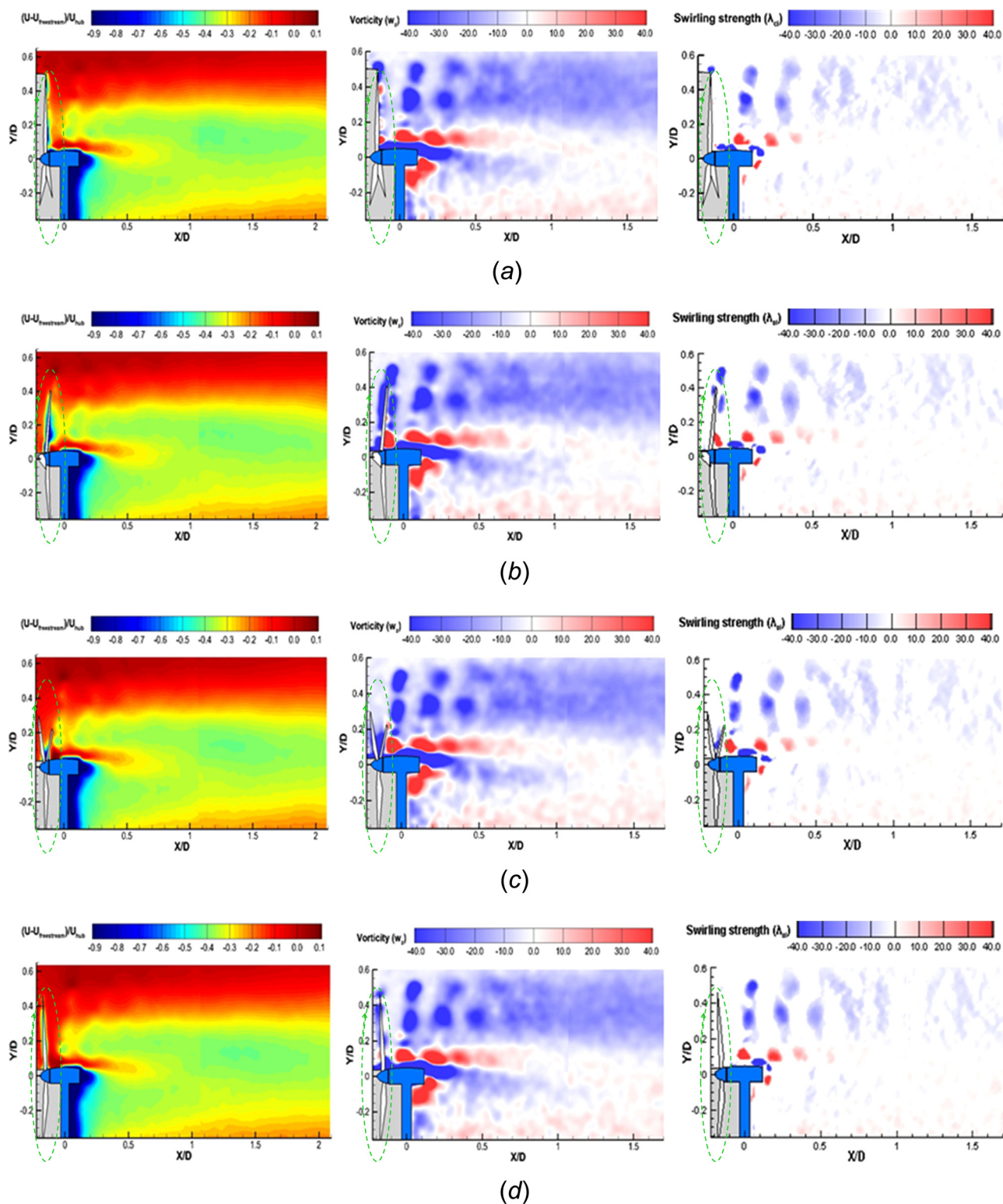
Fig. 12 Phase-locked PIV measurement results of the wake flow behind the SRWT model: normalized streamwise velocity deficit (*left*), vorticity (*middle*), and swirling strength (*right*): (*a*) at the phase angle of $\phi = 0.0$ deg, (*b*) at the phase angle of $\phi = 30.0$ deg, (*c*) at the phase angle of $\phi = 60.0$ deg, and (*d*) at the phase angle of $\phi = 90.0$ deg

with relatively bigger velocity deficits were found to be more pronounced in the wakes behind the DRWT models. The existence of "wave-shaped" flow structures can be observed at the tip-top height in the turbine wakes behind the wind-turbine models, which are closely related to the formation and periodical shedding

of tip vortices in the turbine wakes as reported in Tian et al. [15] and Hu et al. [19].

As shown in the phase-locked vorticity distributions, the wake flows behind the wind-turbine models are actually very complex vortex flows, which are fully filled with various wake vortex
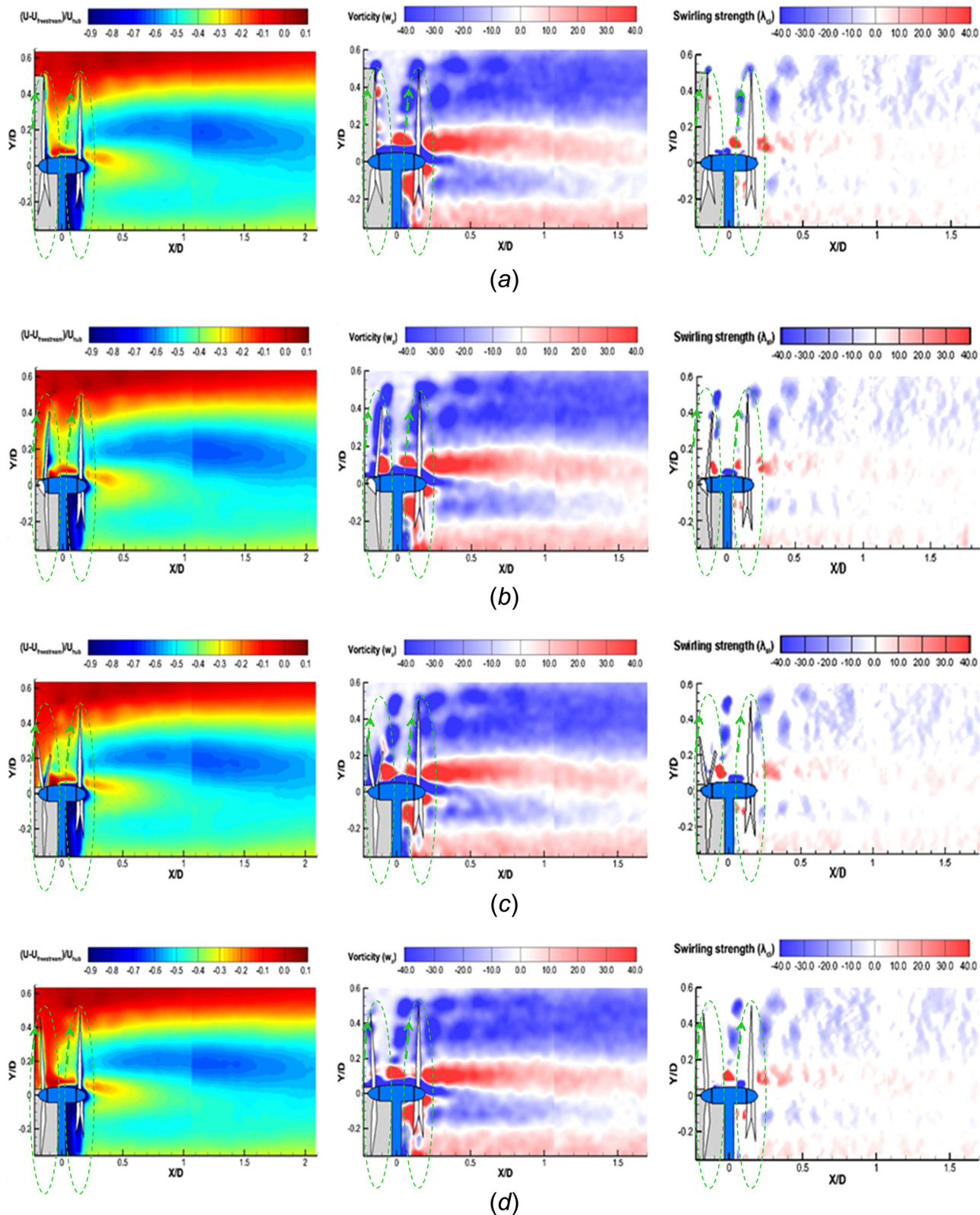
Fig. 13 The phase-locked PIV measurement results of the wake flow behind the co-rotating DRWT model: normalized stream-wise velocity deficit (*left*), vorticity (*middle*), and swirling strength (*right*): (*a*) at the phase angle of $\phi = 0.0\,\mathrm{deg}$, (*b*) at the phase angle of $\phi = 30.0\,\mathrm{deg}$, (*c*) at the phase angle of $\phi = 60.0\,\mathrm{deg}$, and (*d*) at the phase angle of $\phi = 90.0\,\mathrm{deg}$

structures with different spatial and temporal scales. It should also be noted that, because the turbine wake flows also contain strong shearing motions associated with oncoming boundary-layer flow, the vorticity distributions given in Figs. 12–14 will contain

information not only about the unsteady wake vortex structures, but also the strong shearing motions in the wake flows. It will be very difficult, if not impossible, to distinguish between strong shearing motions and the swirling motions of the wake vortex
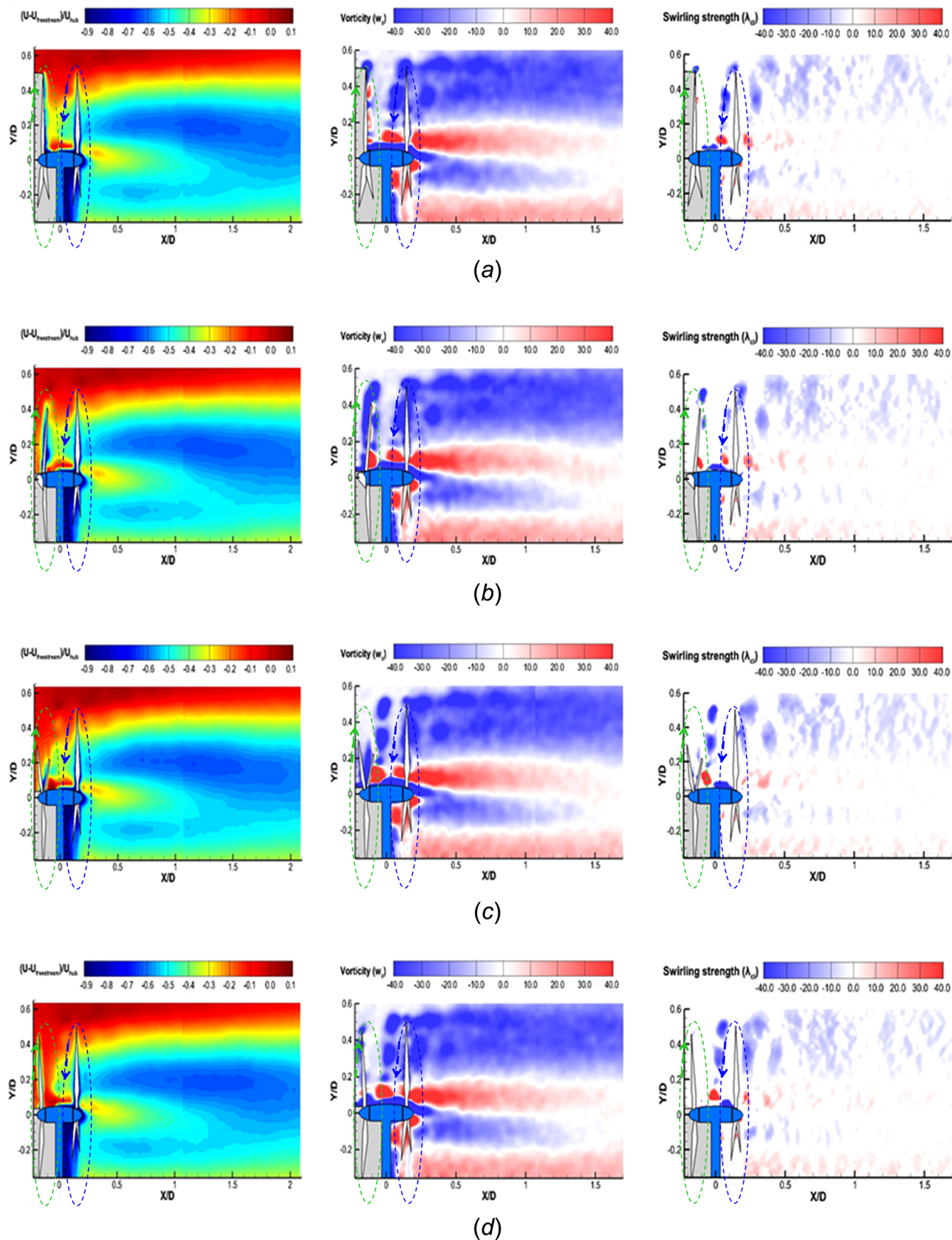
Fig. 14 The phase-locked PIV measurement results of the wake flow behind the counter-rotating DRWT model: normalized streamwise velocity deficit (*left*), vorticity (*middle*), and swirling strength (*right*): (*a*) at the phase angle of $\phi = 0.0$ deg, (*b*) at the phase angle of $\phi = 30.0$ deg, (*c*) at the phase angle of $\phi = 60.0$ deg, and (*d*) at the phase angle of $\phi = 90.0$ deg
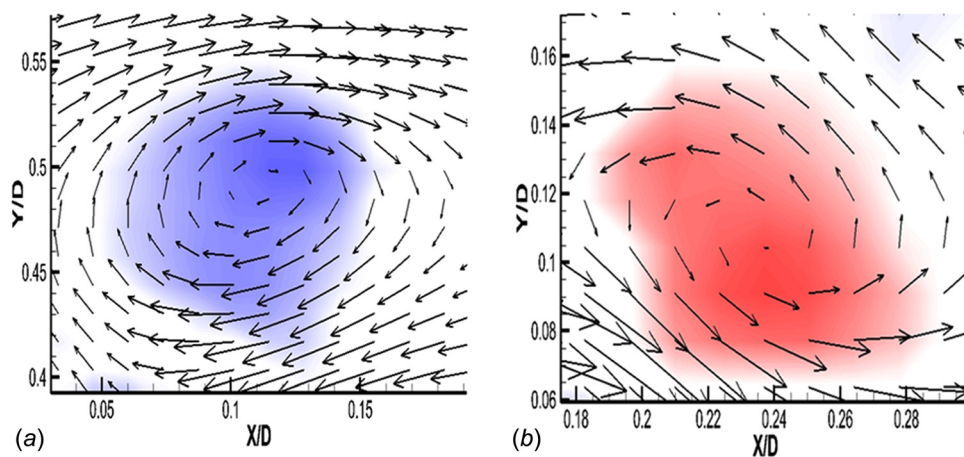
Fig. 15 The relative velocity vectors in the vicinity of vortices in the wake of the SRWT model: (*a*) tip vortex, and (*b*) root vortex

structures. Following the work of Zhou et al. [23], swirling strength, which is the imaginary part of the complex eigenvalue of the velocity gradient tensor, was used in the present study to distinctly visualize the vortex structures in the turbine wake flows.

As shown clearly in the swirling strength distributions given in Figs. 12–14, tip vortices would be induced at the tips of the premarked turbine blades at the phase angle of $\phi = 0.0$ deg. As the phase angle increases, although the premarked turbine blades rotate out of the vertical PIV measurement plane, the tip vortices were found to shed from the tips of the turbine rotor blades. While moving downstream, the tip vortices were found to align nicely with other tip vortices induced by the other rotor blades to form moving tip vortex arrays in the wake flows. Interestingly, an additional row of concentrated vortex structures were also found to be generated at the inboard of the turbine blades at approximately 50%–60% span of the rotor blades. The vortex structures were found to move outward with the expansion of the wake flow as they move downstream, and finally merge with the tip vortex structures and dissipated eventually further downstream. Similar vortex structures at approximately 50%–60% span of the rotor blades were also observed by Tian et al. [15], Hu et al. [19], and Whale et al. [24] in their experimental studies to examine the evolution of unsteady wake vortex structures in turbine wake flows. In addition to the tip vortices and root vortices shedding periodically at the tips and roots of the turbine blades, unsteady vortex structures were also found be generated on the upper and lower surfaces of the turbine nacelles as well as the von Karman vortex streets shedding from the turbine towers. The characteristics in the wake flows behind the wind-turbine models were found to be dominated by the evolution (i.e., formation, shedding, and breakdown) of the unsteady wake vortices.

From the comparisons of the phase-locked PIV measurement results given in Figs. 12–14, it also can be seen that the strength of the tip vortices in the wakes behind the DRWT models were found to be stronger in comparison to those of the SRWT case. This is mainly because of the contribution of the term of "dU/dy" in the vorticity equation, which is associated with the vertical velocity gradient in the wake flows. As shown quantitatively in the streamwise velocity deficit distributions given in Figs. 13 and 14, the greater velocity deficits in the wake flows behind the DRWT models would cause greater gradients along the vertical direction in the wake flow, thereby, higher vorticity values for the wake vortices. However, no obvious differences were observed on the strengths of the tip vortices between the co- and counter-rotating DRWT systems. It can also be seen that, in comparison to the SRWT case, the tip vortices would break down earlier in the wake flows behind the DWRT models, which is in good agreement with the flow characteristics revealed from the wake-induced TKE and

Reynolds stress distributions described above. The strength of the root vortices in the near wake of the counter-rotating DRWT system was found to be weaker because of cross-annihilation of the root vortices from the upwind and downwind rotors. As a result, the corresponding wake-induced TKE levels in the near wake close to the turbine hub were found to be lower in the wake of the counter-rotating DRWT model, in comparison to the SRWT and co-rotating DRWT cases as shown in Fig. 10.

As described in Sherry et al. [25], the tip and root vortices behind a wind turbine would contain wake induced velocity components both in the direction of and opposing to the streamwise velocity of the mean wake flow. Figure 15 gives the relative velocity vectors (i.e., after subtracting the local mean velocity at the center of the root or tip vortex) in the vicinity of tip and root vortices in the wake of the SRWT model at the phase angle of $\phi = 0.0$ deg, which can be used to demonstrate the formation of the tip and root vortices clearly.

The unsteady vortex structures generated within the boundary layer above the turbine nacelles, which have an opposite sign with respect to the root vortices, can also observed in the swirling strength distributions given in Figs. 12–14. The observation is found to be in good agreement with the findings reported in Sherry et al. [25]. It should also be noted that Sherry et al. [25] attributed the rapid destruction of the root vortices to the presence of the unsteady vortices with the opposite sign within the nacelle boundary layer.

Conclusions

An experimental study was carried out to investigate the aeromechanics and wake characteristics of DRWTs in either co-rotating or counter-rotating configuration, in comparison to those of a conventional SRWT. The experimental study was performed in a large-scale wind tunnel with scaled SRWT and DRWT models placed in the same oncoming boundary-layer airflows under neutral stability conditions. In addition to measuring the power outputs and dynamic wind loads acting on the model turbines, a high-resolution PIV system was used to make both free-run and phase-locked measurements to quantify the flow characteristics and behavior (i.e., formation, shedding, and breakdown) of the unsteady wake vortices in the turbine wake flows. The detailed flow field measurements were correlated with the power output and dynamic wind-loading measurements to gain further insight into underlying physics for the optimal design of the wind turbines with higher power yield and better durability.

The measurement results revealed that the power production performance of DRWTs along with the mean (i.e., static), and fluctuation amplitudes of the dynamic wind loads acting on the

DRWT models were found to be much higher compared to the conventional SRWT system. Furthermore, the rotational direction of the dual rotors was found to have a significant effect on the aeromechanic performances of the DRWT systems. The counter-rotating DRWT system, in which the two rotors rotate at opposite directions, was found to harvest more energy than the co-rotating DRWT system. This is because of the fact that the second rotor installed in the near wake of the downwind rotor could harness the additional kinetic energy associated with the swirling velocity of the wake flow of the upwind rotor when the two rotors are set to rotate at opposite directions. Although the DRWT systems were found to be able to harvest more wind energy from the same oncoming airflow, the higher static and dynamic wind loads acting on the DRWT systems would result in higher initial capital costs to build DRWT systems, in comparison to a conventional SRWT system.

The free-run PIV measurement results reveal clearly that the counter-rotating DRWT model was found to have the largest velocity deficits in the wake flow, because it can harness more energy from the oncoming boundary-layer wind, in comparison to the SRWT and co-rotating DRWT models. The regions with relatively higher Reynolds shear stress and wake-induced TKE levels were found to concentrate mainly on the top tip levels of the wake flows, which is in good agreement with previous studies. Although the DRWT systems were found to produce much higher Reynolds shear stress and wake-induced TKE at the top tip level compared to the SRWT system, no obvious differences were observed between the co-rotating and counter-rotating DRWT models. The higher Reynolds shear stress and wake-induced TKE levels in wakes behind the DRWT systems would promote a faster vertical transport of kinetic energy by entraining more high-speed airflow from above to recharge the wakes flow behind the DRWT models, resulting in much faster recovery of the velocity deficits in the wakes behind the DRWT models than that behind the SRWT model.

The phase-locked PIV measurement results reveal that turbine wake flows are actually very complex vortex flows, which are fully filled with various wake vortex structures with different spatial and temporal scales. In addition to the tip vortices and root vortices shedding periodically at the tips and roots of the turbine blades, unsteady vortex structures were also found to be generated on the upper and lower surfaces of the turbine nacelles as well as the von-Karman vortex streets shedding from the turbine towers. The wake characteristics behind the wind-turbine models were found to be dominated by the behavior (i.e., formation, shedding, dissipation, and breakdown) of the unsteady wake vortices shedding from the rotating blades, nacelles, and towers of the wind turbines. It was also found that the strength of the tip vortices in the turbine wakes behind the DRWT models was found to be stronger than that of the SRWT model. The tip vortices behind the DWRT models were also found to break down earlier to cause higher Reynolds stress and the wake-induced TKE levels in the near wakes behind the DRWT model.

Acknowledgment

Nomenclature

ABL = atmospheric boundary layer
D = rotor diameter of the turbine
DRWT = dual-rotor wind turbine
H = hub height of the turbine model
HAWT = horizontal axis wind turbine
L = spacing between the rotors
PIV = particle image velocimetry
R_{uv} = Reynolds shear stress
SRWT = single-rotor wind turbine
TKE = turbulent kinetic energy
TSR = tip speed ratio
U_{hub} = hub height streamwise velocity
w_z = vorticity (out of plane)
λ_{ci} = swirling strength
ϕ = phase angle of the turbine blade

References

[1] Betz, A., 1919, "Schraubenpropeller mit Geringstem Energieverlust (Ship Propellers with Minimum Loss of Energy)," Ph.D. thesis, University of Göttingen, Göttingen, Germany.

[2] Okulov, V. L., and Sørensen, J. N., 2008, "Refined Betz Limit for Rotors With a Finite Number of Blades," Wind Energy, **11**(4), pp. 415–426.

[3] Sharma, A., and Frere, A., 2009, "Aerodynamic Efficiency Entitlement Study of a Horizontal Axis Wind Turbine," Internal Report, General Electric Global Research Center, Schenectady, NY.

[4] Rosenberg, A., Selvaraj, S., and Sharma, A., 2014, "A Novel Dual-Rotor Turbine for Increased Wind Energy Capture," J. Phys.: Conf. Ser., **524**(1), p. 012078.

[5] Newman, B. G., 1986, "Multiple Actuator-Disk Theory for Wind Turbines," J. Wind Eng. Ind. Aerodyn., **24**(3), pp. 215–225.

[6] Appa, K., 2002, "Counter Rotating Wind Turbine System," Technical Report, Energy Innovations Small Grant (EISG) Program, Sacramento, CA.

[7] Jung, S. N., No, T. S., and Ryu, K. W., 2005, "Aerodynamic Performance Prediction of a 30 kW Counter-Rotating Wind Turbine System," Renewable Energy, **30**(5), pp. 631–644.

[8] Habash, R. W. Y., Groza, V., Yang, Y., Blouin, C., and Guillemette, P., 2011, "Performance of a Contra Rotating Small Wind Energy Converter," ISRN Mech. Eng., **2011**, p. 828739.

[9] Shen, W. Z., Zakkam, V. A. K., Sørensen, J. N., and Appa, K., 2007, "Analysis of Counter-Rotating Wind Turbines," J. Phys.: Conf. Ser., **75**(1), p. 012003.

[10] Zhou, Y., and Kareem, A., 2002, "Definition of Wind Profiles in ASCE 7," J. Struct. Eng., **128**(8), pp. 1082–1086.

[11] Jain, P., 2007, Wind Energy Engineering, McGraw-Hill, New York.

[12] Hansen, K. S., Barthelmie, R. J., Jensen, L. E., and Sommer, A., 2012, "The Impact of Turbulence Intensity and Atmospheric Stability on Power Deficits Due to Wind Turbine Wakes at Horns Rev Wind Farm," Wind Energy, **15**(1), pp. 183–196.

[13] Tong, W., 2002, Wind Power Generation and Wind Turbine Design, WIT Press, Billerica, MA.

[14] Yuan, W., Tian, W., Ozbay, A., and Hu, H., 2014, "An Experimental Study on the Effects of Relative Rotation Direction on the Wake Interferences Among Tandem Wind Turbines," Sci. China—Phys. Mech. Astron., **57**(5), pp. 935–949.

[15] Tian, W., Ozbay, A., and Hu, H., 2014, "Effects of Incoming Surface Wind Conditions on the Wake Characteristics and Dynamic Wind Loads Acting on a Wind Turbine Model," Phys. Fluids, **26**(12), p. 125108.

[16] Wilson, R. E., 1994, "Aerodynamic Behavior of Wind Turbines," Wind Turbine Technology: Fundamental Concepts of Wind Turbine Engineering, D. A. Spera, ed., ASME, New York, pp. 215–282.

[17] Alfredsson, P. H., Dahlberg, J. A., and Vermeulen, P. E. J., 1982, "A Comparison Between Predicted and Measured Data From Wind Turbine Wakes," Wind Eng., **6**(3), pp. 149–155.

[18] Chamorro, L. P., Arndt, R. E. A., and Sotiropoulos, F., 2011, "Reynolds Number Dependence of Turbulence Statistics in the Wake of Wind Turbines," Wind Energy, **15**(5), pp. 733–742.

[19] Hu, H., Yang, Z., and Sarkar, P., 2012, "Dynamic Wind Loads and Wake Characteristics of a Wind Turbine Model in an Atmospheric Boundary Layer Wind," Exp. Fluids, **52**(5), pp. 1277–1294.

[20] Vermeer, L. J., Sørensen, J. N., and Crespo, A., 2003, "Wind Turbine Wake Aerodynamics," Prog. Aerosp. Sci., **39**(6–7), pp. 467–510.

[21] Chamorro, L. P., and Porte-Agel, F., 2009, "A Wind-Tunnel Investigation of Wind-Turbine Wakes: Boundary Layer Turbulence Effects," Boundary Layer Meteorol., **132**(1), pp. 129–149.

[22] Meyers, J., and Meneveau, C., 2013, "Flow Visualization Using Momentum and Energy Transport Tubes and Applications to Turbulent Flow in Wind Farms," J. Fluid Mech., **715**, pp. 335–358.

[23] Zhou, J., Adrian, R. J., Balachandar, S., and Kendall, T. M., 1999, "Mechanisms for Generating Coherent Packets of Hairpin Vortices in Channel Flow," J. Fluid Mech., **387**, pp. 353–396.

[24] Whale, J., Anderson, C. G., Bareiss, R., and Wagner, S., 2000, "An Experimental and Numerical Study of the Vortex Structure in the Wake of a Wind Turbine," J. Wind Eng. Ind. Aerodyn., **84**(1), pp. 1–21.

[25] Sherry, M., Sheridan, J., and Lo Jacono, D., 2013, "Characterization of a Horizontal Axis Wind Turbine's Tip and Root Vortices," Exp. Fluids, **54**(3), p. 1417.